

1 This document is the Accepted Manuscript version of a Published Work that appeared in final form in RSC  
2 Advances, copyright © RSC after peer review and technical editing by the publisher.  
3 To access the final edited and published work see  
4 <http://pubs.rsc.org/en/content/articlelanding/2016/ra/c6ra18899k#!divAbstract>

5

6 **Photocatalytic WO<sub>3</sub>/TiO<sub>2</sub> nanowires: WO<sub>3</sub> polymorphs influencing the Atomic Layer**  
7 **Deposition of TiO<sub>2</sub>**

8  
9 **Dávidné Nagy<sup>1,2</sup>, Tamás Firkala<sup>2</sup>, Eszter Drotár<sup>3</sup>, Ágnes Szegedi<sup>3</sup>, Krisztina László<sup>4</sup> and**  
10 **Imre Miklós Szilágyi<sup>2,5</sup>**

11  
12 <sup>1</sup>Institute for Materials and Processes, School of Engineering, The University of Edinburgh,  
13 The King's Buildings, Mayfield Road, Edinburgh, EH9 3JL, United Kingdom

14 <sup>2</sup>Department of Inorganic and Analytical Chemistry, Budapest University of Technology and  
15 Economics, Szent Gellért tér 4., Budapest, H-1111, Hungary

16 <sup>3</sup>Hungarian Academy of Sciences, Institute of Materials and Environmental Chemistry,  
17 Magyar tudósok körútja 2., Budapest, H-1117, Hungary

18 <sup>4</sup>Department of Physical Chemistry and Materials Science, Budapest University of  
19 Technology and Economics, Budafoki út 8., Budapest, H-1111, Hungary

20 <sup>5</sup>MTA-BME Technical Analytical Research Group of the Hungarian Academy of Sciences,  
21 Szent Gellért tér 4., Budapest, H-1111, Hungary

22  
23 **Abstract**

24  
25 50-70 nm hexagonal (h-) and 70-90 nm monoclinic (m-) WO<sub>3</sub> nanoparticles (NPs) were  
26 prepared by controlled annealing of (NH<sub>4</sub>)<sub>x</sub>WO<sub>3</sub> in air at 470 and 600 °C, respectively. In  
27 addition, 5-10 nm thick and several micrometer long h-WO<sub>3</sub> nanowires (NWs) were obtained  
28 by microwave hydrothermal synthesis at 160 °C with Na<sub>2</sub>WO<sub>4</sub>, HCl and (NH<sub>4</sub>)<sub>2</sub>SO<sub>4</sub> as  
29 starting materials. TiO<sub>2</sub> was deposited on h-WO<sub>3</sub> NWs by atomic layer deposition (ALD) at  
30 300 °C using Ti(<sup>i</sup>OPr)<sub>4</sub> and H<sub>2</sub>O as precursors. The as-prepared materials were studied by  
31 TG/DTA-MS, XRD, Raman, SEM-EDX, TEM, ellipsometry, UV-Vis, and their  
32 photocatalytic activity was also tested by the photodecomposition of aqueous methyl orange.  
33 Our study is the first evidence of diverse ALD nucleation on various WO<sub>3</sub> polymorphs, since  
34 on h-WO<sub>3</sub> NWs TiO<sub>2</sub> nucleated only as particles, whereas on m-WO<sub>3</sub> conformal TiO<sub>2</sub> film  
35 was formed, explained by the different surface OH coverage of h- and m-WO<sub>3</sub>. The h-WO<sub>3</sub>  
36 NWs had significantly higher photocatalytic activity compared to h-WO<sub>3</sub> NPs, and similar  
37 performance as m-WO<sub>3</sub> NPs. By adding TiO<sub>2</sub> to h-WO<sub>3</sub> NWs by ALD method, the  
38 photocatalytic performance increased by 65 %, showing clearly the uniqueness of ALD to  
39 obtain superior oxide composite photocatalysts.

40  
41  
42  
43  
44  
45  
46  
47  
48  
49  
50  
51  
52  
53  
54  
55  
56  
57  
58  
59  
60  
61  
62  
63  
64  
65  
66  
67  
68  
69  
70  
71  
72  
73

## Introduction

Water scarcity and the purity of available water resources around the world are concerning issues of our century.<sup>1, 2</sup> Semiconductor photocatalysis received substantial attention recently to address environmental remediation challenges such as purifying water sources.<sup>3-7</sup> It was presented that using solar energy the purification of water is possible from toxic compounds such as certain pharmaceutical drugs, bacteria or herbicides...etc.<sup>8, 9</sup> Among semiconductor oxides TiO<sub>2</sub> is one of the most studied photocatalyst since its valence and conductance energy levels are suitable for both oxidation and reduction of water molecules (water splitting)<sup>10-17</sup>. However, the utilization of TiO<sub>2</sub> is hugely limited by its restricted light absorption properties to the UV range. Therefore, besides TiO<sub>2</sub>, the photocatalytic activity of several other semiconductor oxides was also studied (eg. V<sub>2</sub>O<sub>5</sub>, WO<sub>3</sub>, ZnO, ZrO<sub>2</sub>)<sup>18-24</sup>. Nanostructured WO<sub>3</sub> can absorb part of the Visible spectrum, making it the second most studied oxide for Visible-responsive photocatalysis<sup>25</sup>.

Another limiting factor of TiO<sub>2</sub> is the relatively fast recombination of the photo-induced charges. One approach to improve the photocatalytic performance of a semiconductor oxide is forming composite photocatalysts with other semiconductors. An important benefit of forming composite nanostructures could be the reduced recombination rate of the photo-generated charges by effective charge transfer between the two semiconductor oxide. In the case of type II band alignment where one of the nanostructure has both the valence and conduction band energies lower positioned than the respective bands of the counterpart effective separation of the charge carriers can take place.<sup>26</sup> In addition to the production of longer-lived charges, the heterostructure can benefit from Vis activity if a UV active photocatalyst such as TiO<sub>2</sub> is coupled with semiconductor oxides absorbing in the Visible region. TiO<sub>2</sub>/WO<sub>3</sub> is such a system and several studies showed that such nanocomposite heterostructures have superior photocatalytic activities over single semiconductors<sup>27-30</sup>.

It is also known that the photocatalytic activity is a complex function of several factors such as the crystal structure, morphology or optical properties of the material...etc<sup>31, 32</sup> In order to achieve high performance photocatalysts maximizing the specific surface area of the material is a general approach. Therefore, several techniques have been adopted to fabricate nanostructured oxide photocatalysts. Among the reported nanostructures, nanofibers have received immense attention due to their high surface-to-volume ratio, good optical, electric and chemical properties<sup>33, 34</sup>.

74 Previous studies revealed that  $\text{WO}_3/\text{TiO}_2$  1D photocatalysts have huge potential<sup>35-38</sup>.  
75 Unfortunately,  $\text{WO}_3$  is quite difficult to prepare with very small dimensions. The smallest  
76 forms of the most studied  $\text{WO}_3$  polymorph, i.e. monoclinic (m-)  $\text{WO}_3$  have been 10-100 nm  
77 as particles, or 50-200 nm as nanofibers<sup>39-41</sup>. Nevertheless, m- $\text{WO}_3$  is a widespread  
78 photocatalyst. In contrast, the second most important  $\text{WO}_3$  modification, i.e. hexagonal (h-)  
79  $\text{WO}_3$ , has been studied in photocatalysis only once, and its photocatalytic activity was lower  
80 compared to m- $\text{WO}_3$ .<sup>42</sup> It was explained by that unlike the completely oxidized m- $\text{WO}_3$ , h-  
81  $\text{WO}_3$  always contain some cation (e.g.  $\text{Na}^+$ ,  $\text{K}^+$ ,  $\text{NH}_4^+$ ) impurities in its hexagonal channels,  
82 which are vital for stabilizing the metastable structure.<sup>43, 44</sup> Besides, h- $\text{WO}_3$  contains also  
83 partially reduced W atoms, which may serve as recombination centers during the  
84 photocatalytic reaction, decreasing the activity.<sup>43</sup> However, h- $\text{WO}_3$  has been prepared  
85 recently in the form of very fine nanowires with ca. 5-10 nm thickness, which is a very  
86 promising morphology for photocatalysis, but unfortunately their photocatalytic properties  
87 have not been tested yet.

88 Recently it was reported that m- $\text{WO}_3/\text{TiO}_2$  core/shell nanofibers, where the shell layer was  
89 deposited by atomic layer deposition (ALD), had excellent photocatalytic properties due to  
90 the synergy of  $\text{WO}_3$  and  $\text{TiO}_2$ <sup>45</sup>. ALD is based on successive, alternating surface controlled  
91 reactions from the gas phase to produce highly conformal and uniform thin films with  
92 thickness control of sub-nanometer precision. Thus, ALD provides new strategies in  
93 modifying the properties of nanoscaled materials and new synthetic routes to novel  
94 nanostructures<sup>46-52</sup>.

95 In the above example the m- $\text{WO}_3$  nanofibers were 200-300 nm thick. Thus, it is logical to  
96 expect better photocatalytic properties, if  $\text{WO}_3$  1D nanostructures with even smaller  
97 dimensions can be used as substrates. The now available 5-10 nm thick h- $\text{WO}_3$  fibers are  
98 good candidates for employing in  $\text{WO}_3/\text{TiO}_2$  photocatalysts with improved properties.

99 In this study, we obtained h- $\text{WO}_3$  NWs by microwave assisted hydrothermal synthesis at 160  
100 °C with  $\text{Na}_2\text{WO}_4$ , HCl and  $\text{Na}_2\text{SO}_4$  as starting materials. ALD was the method of choice to  
101 put  $\text{TiO}_2$  onto the h- $\text{WO}_3$  nanowires, since it has the capability to deposit very thin layers on  
102 highly structured surfaces. The  $\text{TiO}_2$  layer was deposited at 300 °C using  $\text{Ti}(\text{iOPr})_4$  and  $\text{H}_2\text{O}$   
103 as precursors, and it was designed to have around 3 nm thickness because previous studies  
104 showed that thin  $\text{TiO}_2$  nanolayers could significantly enhance the photo-efficiency of the  
105 nanosized  $\text{WO}_3$ <sup>45</sup>. It must be noted that up to now ALD growth has been done only on m-  
106  $\text{WO}_3$ , but not on h- $\text{WO}_3$ . Since the two polymorphs have different surface properties<sup>42</sup>, this  
107 allowed us to study the characteristics of ALD nucleation on the surface of various  $\text{WO}_3$

108 crystalline structures, which was not yet reported in the literature to the best of our  
109 knowledge.

110 For comparison, we also prepared hexagonal (h-) and monoclinic (m-)  $\text{WO}_3$  nanoparticles  
111 (NPs) by controlled annealing of  $(\text{NH}_4)_x\text{WO}_3$  in air at 470 and 600 °C, respectively. In  
112 addition, we prepared an m- $\text{WO}_3/\text{TiO}_2$  composite by annealing the h- $\text{WO}_3/\text{TiO}_2$  sample at  
113 600 °C in air. It is well established that at this temperature the h- $\text{WO}_3$  structure transforms  
114 into m- $\text{WO}_3$ . Usually when m- $\text{WO}_3$  is formed thermally from nanostructured precursors, it  
115 will be present in the form of 50-200 nm particles<sup>53</sup>. However, we aimed to test whether the  
116  $\text{TiO}_2$  coating might prevent the morphology change, and m- $\text{WO}_3/\text{TiO}_2$  with nanowire  
117 morphology could be obtained.

118 The obtained materials were studied by TG/DTA-MS, XRD, Raman, SEM-EDX, TEM,  
119 ellipsometry, UV-Vis, and their photocatalytic activity was tested by UV-Vis through the  
120 photo-bleaching of aqueous methyl orange.

121

## 122 **Experimental**

123

124 *Preparation methods.* Hexagonal (h-) and monoclinic (m-)  $\text{WO}_3$  nanoparticles (NPs) were  
125 prepared by annealing hexagonal ammonium tungsten bronze,  $(\text{NH}_4)_x\text{WO}_{3-y}$  in air at 470 °C  
126 and 600 °C, respectively<sup>34,54</sup>.

127 For the preparation of h- $\text{WO}_3$  nanowires (NWs) a microwave-assisted hydrothermal synthesis  
128 method was applied<sup>44</sup>. 1.5 g  $\text{Na}_2\text{WO}_4 \cdot 2\text{H}_2\text{O}$  was dissolved in 33.75 ml  $\text{H}_2\text{O}$ , then under  
129 stirring 3.75 ml 3 M HCl was added dropwise, and finally 22.5 ml 0.5 M  $(\text{NH}_4)_2\text{SO}_4$  was  
130 introduced. The as-prepared solution was heated to 160 °C in 20 min, and then kept at 160 °C  
131 for 3 hours in a Synthos 3000 Anton Paar microwave reactor. The solid reaction product was  
132 centrifuged, washed two times with water, once with ethanol, and again two times with water.  
133 In each washing step, 45 ml solvent was poured over the crystals; the dispersion was stirred  
134 for 1 min, and centrifuged for 5 min at 6000 1/min. Finally, the as-prepared h- $\text{WO}_3$  NWs  
135 were dried at 80 °C for 12 hours. The yield was 64 %.

136 The h- $\text{WO}_3/\text{TiO}_2$  nanowire composite was prepared by depositing a  $\text{TiO}_2$  nanolayer onto the  
137 surface of the as-prepared h- $\text{WO}_3$  NWs by atomic layer deposition (ALD). The ALD reaction  
138 was carried out at 300 °C in a Picosun SUNALE R-100 type reactor. 100 ALD cycles were  
139 applied using  $\text{Ti}(\text{O}^i\text{Pr})_4$  (60 °C evaporation temperature) and  $\text{H}_2\text{O}$  as precursors, with 1 s  
140 pulse and 30 s purge times for both precursors.

141 The m-WO<sub>3</sub>/TiO<sub>2</sub> composite sample was obtained by annealing the h-WO<sub>3</sub>/TiO<sub>2</sub> sample at  
142 600 °C in air.

143

144 *Characterization methods.* Thermal analysis was used to investigate the influence of washing  
145 steps during the h-WO<sub>3</sub> NW preparation and to check the thermal stability of as-synthesized  
146 h-WO<sub>3</sub> NWs. For this an STD 2960 simultaneous TG/DTA device (TA Instruments Inc.) was  
147 used, which was on-line coupled to a Thermostar GSD 200 quadruple mass spectrometer  
148 (Balzers Instruments) through a heated (200 °C), 100 % silanated quartz capillary (D = 0.15  
149 mm). During the TG/DTA-MS measurements, samples (ca. 100 mg) were heated in a Pt  
150 crucible at 10 °C/min heating rate in flowing air (130 ml/min). The fragments of the evolved  
151 gases were monitored by Multiple Ion Detection (MID) mode in the 1-64 m/z range.

152 The crystal phases were determined by recording the XRD pattern of the samples by a  
153 PANalytical X'pert Pro MPD X-ray diffractometer using Cu K $\alpha$  radiation.

154 The Raman spectra provided further information on the crystal structure and the bonds. A  
155 Jobin-Yvon Labram type spectrophotometer equipped with an Olympus BX-41 microscope  
156 was used. For excitation source a frequency-doubled Nd-YAG laser (532 nm) was employed.  
157 The scattered photons were collected by a CCD type detector.

158 To investigate the optical properties of the catalysts, UV-Vis diffuse reflectance spectra were  
159 recorded by a Cary 100 UV-Vis spectrophotometer equipped with a DRA-CA-30I type  
160 integration sphere.

161 For the study of the morphology and composition, SEM-EDX and TEM measurements were  
162 applied. A LEO 1540XB type RÖNTEC FEG SEM microscope equipped with a Quantax  
163 EDX detector was used for the SEM-EDX recordings. The TEM images were provided by a  
164 FEI Morgagni 268D type TEM microscope employing a tungsten cathode.

165 For determining the specific surface area of the photocatalysts, the BET model was used. The  
166 measurement was conducted in a NOVA 2000E type (Quantachrome, USA) device at the  
167 temperature of liquid nitrogen applying N<sub>2</sub> as an adsorbent gas.

168 For estimating the ALD TiO<sub>2</sub> film thickness, a TiO<sub>2</sub> film was deposited on a Si wafer by  
169 ALD, using 300 cycles and the same precursors, pulse and purge times, as in the case of h-  
170 WO<sub>3</sub> NW substrates. The film thickness was determined by ellipsometry. The spectra were  
171 recorded by a Woollam M-2000DI ellipsometer between 400 and 1500 nm.

172

173 *Photocatalysis.* The photocatalytic efficiencies of the as-prepared catalysts were tested in the  
174 photo-bleaching reaction of methyl-orange (MO). The concentration of the catalyst and the

175 methyl orange were 100 mg/350 ml and 10 mg/350 ml, respectively. A Heraus TQ 150  
176 mercury immersion lamp (radiation flux,  $\Phi$ : 200-600 nm 47 W, strongest spectral lines: 254  
177 nm: 4W, 313 nm: 4.3 W, 366 nm: 6.4 W, 405 nm: 3.2W, 436 nm: 4.2 W, 546 nm: 5.1 W, 577  
178 nm: 4.7 W) was applied in a Heraus type cylindrical glass photo-reactor. The experiments  
179 were conducted under oxygen bubbling at room temperature assured by the continuous water  
180 circulation through the cooling jacket of the lamp. At first the solution was kept in dark for 15  
181 min, to reach the adsorption equilibrium between the catalyst and the dye. Then the lamp was  
182 switched on and 3 ml samples were taken in every 30 min using a syringe equipped with  
183 filter (Sigma Aldrich, Iso-Disc, PTFE, 0.45  $\mu$ m pore size membrane). The decline of the MO  
184 concentration was followed by a Jasco V-550 type UV-Vis spectrophotometer at 465 nm.

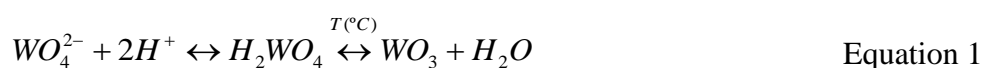
185

## 186 **Results and discussion**

187

188 *Formation mechanism of h-WO<sub>3</sub> nanowires.* The fabrication of nano-sized WO<sub>3</sub> by wet-  
189 chemical synthesis approaches such as hydrothermal (HT) synthesis is a popularly applied  
190 method for cheap and versatile nanostructure formulation.<sup>44, 55</sup> To direct crystal growth in  
191 HT synthesis various structure directing agents were presented in the literature from simple  
192 inorganic salts like Na<sub>2</sub>SO<sub>4</sub>, NH<sub>4</sub>NO<sub>3</sub> to complex organic structures like oxalic acid or poly-  
193 ethylene glycol.<sup>33, 55, 56</sup> To fabricate delicate h-WO<sub>3</sub> nanowires in this paper (NH<sub>4</sub>)<sub>2</sub>SO<sub>4</sub> was  
194 used following an earlier report.<sup>44</sup> It is believed that the capping agents such as (NH<sub>4</sub>)<sub>2</sub>SO<sub>4</sub>  
195 dictate anisotropic 1D growth by selectively binding to specific crystal facets of the initial  
196 crystal nuclei of WO<sub>3</sub>. The adsorption of capping agents increases the surface energy of the  
197 selected facets leading to inhibited crystal growth rates and resulting in the formation of 1D  
198 nanostructures.<sup>44</sup> It is also known that several other factors may contribute to the morphology  
199 and crystal phases of the final nanomaterials such as time, temperature or the pH.<sup>31, 55, 57</sup> This  
200 latter one plays an especially important role in the formation of WO<sub>3</sub> since H<sup>+</sup> is essential to  
201 form tungstic acid from the selected tungsten precursor which is typically a tungstate. Then  
202 WO<sub>3</sub> is formed according to Equation 1.

203



204

205 *Thermal analysis.* The role of washing steps in reaching pure h-WO<sub>3</sub> nanowires after the  
206 microwave hydrothermal reactions was studied by TG/DTA-MS measurement. The results  
207 (presented in detail in the Supporting information) confirmed that washing steps were  
208 effective and removed all precursors and reactants. The as-prepared, non-washed, only dried  
209 h-WO<sub>3</sub> NW samples contained significant amount from not used reagents, i.e. (NH<sub>4</sub>)<sub>2</sub>SO<sub>4</sub>,  
210 HCl, and water as well, from which various gaseous products were detected in air, e.g. H<sub>2</sub>O,  
211 NH<sub>3</sub>, from the decomposition of NH<sub>4</sub><sup>+</sup>, NO and N<sub>2</sub>O from the combustion of NH<sub>3</sub>, HCl, SO  
212 and SO<sub>2</sub> from the decomposition of SO<sub>4</sub><sup>2-</sup> <sup>58</sup>. (Table S1). When the sample was annealed,  
213 until 100 °C small amount of adsorbed H<sub>2</sub>O was released in an endothermic reaction (Fig.  
214 S1-S2). Then between 150-300 °C H<sub>2</sub>O and NH<sub>3</sub> evolved accompanied by an endothermic  
215 heat effect, whereas between 300-450 °C H<sub>2</sub>O, NH<sub>3</sub>, NO<sub>x</sub> and SO<sub>x</sub> gases were detected. The  
216 combustion of NH<sub>3</sub> was an endothermic reaction, which changed the DTA curve to  
217 endothermic <sup>59</sup>. HCl was released above 450 °C, accompanied by further release of SO<sub>2</sub>.  
218 After the washing steps (Fig. S3-S4), all impurities were removed, and accordingly the total  
219 mass loss until 900 °C decreased from 18.2 % to 5.8 %. Now only the release of water was  
220 observed in two endothermic reactions between 25-200 and 200-450 °C. The metastable  
221 hexagonal WO<sub>3</sub> framework was transformed into the thermodynamically stable m-WO<sub>3</sub> at  
222 503 °C in an exothermic reaction. The results confirmed the importance of proper washing  
223 steps after the microwave hydrothermal reaction in order to obtain pure h-WO<sub>3</sub> nanowires.  
224 The thermal analysis also showed that the cleaned, pure h-WO<sub>3</sub> was stable until 500 °C,  
225 therefore performing the ALD reaction at 300 °C was safe.  
226 After the ALD reaction performed at 300 °C-on and 10<sup>3</sup> Pa vacuum the h-WO<sub>3</sub> NWs lost  
227 considerable amount of adsorbed and structural water (only 2.5 % mass loss) (Fig. S6-S7).  
228 The exothermic DTA peak belonging to the hexagonal-monoclinic WO<sub>3</sub> transformation was  
229 at 506 °C.  
230  
231 *XRD.* The XRD patterns (Fig. 1) served information about the crystalline structure of the  
232 samples. No crystalline impurities were detected in any of the samples. All reflection peaks  
233 of h-WO<sub>3</sub> NPs were assigned to pure h-WO<sub>3</sub> (ICDD 33-1387). The h-WO<sub>3</sub> NWs exhibited  
234 well-defined and intense diffraction peaks supposing high crystallinity of the sample. The  
235 crystalline phase was confirmed to be pure h-WO<sub>3</sub>. The XRD pattern of m-WO<sub>3</sub> NPs was  
236 interpreted as pure monoclinic WO<sub>3</sub> (ICDD 43-1035).



237 In the diffraction pattern of h-WO<sub>3</sub>/TiO<sub>2</sub> nanocomposite (Fig. 1) only the h-WO<sub>3</sub> phase could  
238 be identified (ICDD 33-1387). The characteristic reflections of TiO<sub>2</sub> could not be detected in  
239 the XRD pattern due to the very thin TiO<sub>2</sub> layer (aimed to be less than 3 nm).

240

241 *Raman.* The crystalline phases of the as-prepared WO<sub>3</sub> nanostructures were confirmed by  
242 their Raman spectra as well (Fig. 2), in agreement with the XRD results. The h-WO<sub>3</sub> NPs  
243 showed well-defined bands characteristic of h-WO<sub>3</sub>. The most intense peak at 785 cm<sup>-1</sup> along  
244 with the bands at 650 and 691 cm<sup>-1</sup> can be associated with the stretching vibration modes of  
245 (O-W-O)<sup>60, 61</sup>. The bands at 263 and 320 cm<sup>-1</sup> can be assigned to bending vibrations of W-O-  
246 W, whereas at 186 cm<sup>-1</sup> the lattice vibration mode can be found<sup>60, 62</sup>.

247 The Raman spectrum of h-WO<sub>3</sub> NWs was substantially different from that of the h-WO<sub>3</sub> NPs.  
248 One of the deviances was that the h-WO<sub>3</sub> NW exhibited overlapping bands in the region of  
249 600 and 850 cm<sup>-1</sup>. Another considerable difference was that exclusively in the Raman spectra  
250 of h-WO<sub>3</sub> NWs terminal W=O stretching modes were recognizable in the interval of 925-965  
251 cm<sup>-1</sup><sup>60, 63-65</sup>. These peaks are common for all types of WO<sub>3</sub> hydrates, and in some cases the  
252 appearance of these bands were attributed to surface humidity<sup>43</sup>. The absence of these bands  
253 in the spectra of h-and m-WO<sub>3</sub> NPs can be ascribed to the high temperature treatment at 500  
254 and 650 °C, respectively. *Santato et al.* reported that the W=O stretching modes in the latter  
255 wavenumber interval gradually disappeared by applying increasing annealing temperature in  
256 the synthesis process<sup>63</sup>.

257 The Raman bands of m-WO<sub>3</sub> NPs were in good correspondence with literature values<sup>66</sup>. The  
258 peaks were sharp and well-developed supposing good crystallinity of the sample. The bands  
259 positioned at 806 and 720 cm<sup>-1</sup> can be assigned to stretching (O-W-O) vibrational modes. The  
260 bands at lower wavelength values belong to (O-W-O) deformation modes<sup>60</sup>.

261 The Raman bands of h-WO<sub>3</sub>/TiO<sub>2</sub> nanocomposite (Fig. 2) were broadened, compared to h-  
262 WO<sub>3</sub> NWs. Probably during the ALD deposition some partially reduced W atoms were  
263 produced, either due to the conditions (300 °C, 10<sup>3</sup> Pa vacuum) or to the reaction between the  
264 precursors and the substrate, and therefore the structure became less ordered. The Raman  
265 spectrum is sensitive to the different oxidation states of the atoms due to the change of the  
266 chemical bond strength, which resulted in a small shift of the peak positions involving W  
267 atoms of different oxidations states<sup>42</sup>. In the h-WO<sub>3</sub>/TiO<sub>2</sub> sample the bands involving  
268 completely oxidized (+6) and partially reduced (+5, +4) W atoms overlapped, making the  
269 peaks broader. The presence of partially reduced tungsten atoms was also indicated by the  
270 color change of the sample (it became blue) and by its optical behavior, discussed later. In

271 addition, the terminal W=O stretching modes (above  $900\text{ cm}^{-1}$ ) of the h-WO<sub>3</sub>/TiO<sub>2</sub>  
272 nanocomposite had much lower intensities compared to the substrate h-WO<sub>3</sub> NW. The  
273 occurred ALD nucleation and the applied temperature and pressure could be accounted for  
274 the reduced band intensities.

275 Characteristic bands of TiO<sub>2</sub> could not be observed as the bands of TiO<sub>2</sub> usually become  
276 perceptible above 10 nm film thickness<sup>45</sup>. Similar findings were made by others who found  
277 that 1-5% WO<sub>3</sub> loading in a WO<sub>3</sub>/TiO<sub>2</sub> nanostructure did not show bands for WO<sub>3</sub> due to low  
278 content of WO<sub>3</sub>.<sup>67</sup>

279

280

281 *SEM-EDX, TEM.* Fig. 3 shows the SEM and TEM images of the prepared catalyst. It was  
282 found that the h-WO<sub>3</sub> NPs (Fig. 3a-b) consisted of 50-70 nm nanocrystals. The SEM and  
283 TEM images confirmed the formation of uniform and good quality nanowires for the h-WO<sub>3</sub>  
284 NWs (Fig. 3c-d) being several micrometer long and ca. 5-10 nm thick. On Fig. 3e-f the m-  
285 WO<sub>3</sub> NPs can be viewed, consisting of irregularly-shaped nanoparticles with a characteristic  
286 dimension of 60-90 nm.

287 The EDX elemental analysis revealed that h-WO<sub>3</sub> NWs contained 2.82 atom% of Na beside  
288 W and O atoms, which can be attributed to stabilizing Na ions in the hexagonal channels<sup>43</sup>.

289 SEM-EDX results were also obtained about the effectiveness of the washing steps. On the  
290 SEM image of the as-prepared, non-washed, dried h-WO<sub>3</sub> NW sample micrometer scale  
291 particles of the not used reactants can be also seen, and EDX analysis confirmed the presence  
292 of N, Cl and S, besides O, Na and W (Fig. S5).

293 In the h-WO<sub>3</sub>/TiO<sub>2</sub> NWs the SEM and TEM images (Fig. 4a-b) revealed that the TiO<sub>2</sub> was  
294 successfully deposited onto the surface of h-WO<sub>3</sub> NWs in the form of individual  
295 nanoparticles. The TiO<sub>2</sub> nanoparticles had the diameter of around 5-10 nm, which  
296 corresponds to double thickness obtained by ellipsometry data, and is rationalized by the 3D  
297 growth of the TiO<sub>2</sub> particles. This is in agreement with expectations, as in the case of  
298 nanoparticle nucleation a 3D ALD growth is taking place. EDX showed 2.64 atom% Ti in the  
299 h-WO<sub>3</sub>/TiO<sub>2</sub> sample, and confirmed the successful deposition of TiO<sub>2</sub> onto the h-WO<sub>3</sub> NWs.

300 It was also investigated whether an m-WO<sub>3</sub>/TiO<sub>2</sub> composite with nanowire morphology could  
301 be obtained by annealing the h-WO<sub>3</sub>/TiO<sub>2</sub> sample. According to SEM and TEM images (Fig.  
302 4c-d), the fine nanowire morphology was lost when h-WO<sub>3</sub> transformed into m-WO<sub>3</sub>. In the  
303 m-WO<sub>3</sub>/TiO<sub>2</sub> composite m-WO<sub>3</sub> was present in the form of 30-50 nm particles, some of them

304 being connected to each other in a line, pointing to their h-WO<sub>3</sub> nanowire origin. The TiO<sub>2</sub>  
305 could be observed as 10 nm particles on the surface of m-WO<sub>3</sub>.

306  
307

308 *BET.* The BET measurements were carried out to compare the specific surface area of the  
309 synthesized WO<sub>3</sub> nanostructures. For h-WO<sub>3</sub> NPs it was found to be 11 m<sup>2</sup>g<sup>-1</sup>.<sup>68</sup> Whereas the  
310 h-WO<sub>3</sub> NWs exhibited a much higher surface area of 101 m<sup>2</sup>g<sup>-1</sup> which is in good agreement  
311 with earlier literature results.<sup>44</sup> The almost an order of magnitude higher specific surface area  
312 of the h-WO<sub>3</sub> NWs relative to the h-WO<sub>3</sub> NPs showed the significant effect of the  
313 morphology in the specific surface area which is considered to be an important factor in  
314 photocatalysis. The BET surface area of m-WO<sub>3</sub> nanostructure was calculated to be the  
315 lowest among the WO<sub>3</sub> nanostructures with 6.5 m<sup>2</sup>g<sup>-1</sup>.<sup>42</sup>

316

317 *Ellipsometry.* The estimation of the equivalent TiO<sub>2</sub> layer thickness was determined by  
318 ellipsometry on a reference Si wafer. As the native oxide layer on the Si wafer is  
319 approximately 3 nm thick, three times more ALD cycle (300 ALD cycle) were run under the  
320 same condition on the reference wafer than during the preparation of the nanocomposite in  
321 order to make the estimation more accurate. The approximated equivalent TiO<sub>2</sub> thickness  
322 prepared by 100 ALD cycles was calculated as 3.65 nm.

323

324

325 *ALD nucleation determined by the surface properties of WO<sub>3</sub> polymorphs.* Based on SEM  
326 and TEM results, it was found that the TiO<sub>2</sub> nucleation followed a distinct pattern on WO<sub>3</sub>  
327 polymorphs. Earlier it was reported that the ALD-deposited TiO<sub>2</sub> formed a continuous layer  
328 on the surface of electrospun m-WO<sub>3</sub> nanofibers resulting in a core-shell nanocomposite<sup>45</sup>.  
329 Our results revealed that for h-WO<sub>3</sub> nanowires, instead of a continuous layer, the deposited  
330 TiO<sub>2</sub> formed nanoparticle islands. The surface chemistry of the nanostructures plays a key  
331 role in the ALD reaction as the native functional group coverage on the surface serves as first  
332 binding sites for the ALD reaction<sup>69-71</sup>. Most probably, the distinct ALD nucleation could be  
333 accounted for the different surface OH<sup>-</sup> group density of the WO<sub>3</sub> polymorphs. *Szilagyi et al*  
334 reported that based on the XPS spectra the amount of surface OH<sup>-</sup> group was 0.52 % for the  
335 h-WO<sub>3</sub> NPs and 0.70 % for m-WO<sub>3</sub> NPs<sup>42</sup>. The nucleation of TiO<sub>2</sub> nanoparticles on the  
336 surface of h-WO<sub>3</sub> as opposed to continuous film construction, is probably due to the less  
337 available nucleation sites.

338 *UV-Vis absorption.* All WO<sub>3</sub> nanostructures regardless of the crystal phase exhibited pale  
339 yellow colour, however it was found that h-WO<sub>3</sub>/TiO<sub>2</sub> NWs nanocomposite turned into blue  
340 after the ALD reaction. Solid phase UV/Vis diffuse reflectance (DR) spectra were recorded  
341 and analyzed to reveal the optical behavior of the nanostructures and help to understand the  
342 reason for the colour differences. The DR spectra is shown in Fig. 5.

343 It was observed that the h-WO<sub>3</sub> NWs and NPs exhibited a sharp drop of the absorption  
344 around 460 nm and 478 nm respectively. Similarly, m-WO<sub>3</sub> NPs showed an absorption  
345 threshold at about 485 nm. These values are typical band edges for nanostructured WO<sub>3</sub>.<sup>56, 72</sup>  
346 It is believed that h-WO<sub>3</sub> nanostructures typically exhibit higher energy band values  
347 (therefore appears at lower wavelength) due to structural differences.<sup>73</sup>

348 For the h-WO<sub>3</sub>/TiO<sub>2</sub> nanocomposite it was noted that although TiO<sub>2</sub> has a typical absorption  
349 threshold around 390-410 nm,<sup>74</sup> the nanocomposite still exhibited absorption in the whole Vis  
350 range. Presumably, the enhanced visible absorption arose from the newly generated in-gap  
351 states in the band gap due to the presence of partially reduced W atoms. The reduced W  
352 atoms were indicated by Raman spectroscopic results and it is believed to be caused by the  
353 high temperature and vacuum used over the course of ALD reaction. The blue appearance of  
354 the sample is also an indication of the presence of in-gap states in the far-red region of the  
355 Visible spectrum.

356

357

358 *Photocatalysis.* The photo-efficiency of the catalysts was modelled in the photo-bleaching  
359 reaction of methyl orange under UV-Vis light irradiation (Fig. 6). The relative absorbance  
360 was calculated and plotted against time to follow the dye degradation (see on Fig. 6 a)).  
361 Additionally, first-order kinetics could be used to describe the behavior of our data which can  
362 be expressed in the following form:

$$\ln\left(\frac{C}{C_0}\right) = kt \quad \text{Equation 2}$$

363 where C is the dye concentration, C<sub>0</sub> is the initial dye concentration, k is the first-order rate  
364 constant and t is time. To test the repeatability of the photocatalytic results multiple  
365 experiments were performed. It was found that the experimental error has never exceeded  
366 ±4% and was typically 2-3%. The effect of photolysis was negligible under the experimental  
367 conditions. The catalysts after the photocatalytic test did not show any visible change eg. in  
368 their color.

369 It was found that the nanowire morphology could enhance significantly the photoactivity of  
370 h-WO<sub>3</sub> NWs. Compared to the reference h-WO<sub>3</sub> NPs, the h-WO<sub>3</sub> NWs photo-bleached more  
371 than twice as much dye within 4 hours. The enhanced efficiency was reflected on the first-  
372 order rate constant values as well, exhibiting  $1.72 \cdot 10^{-3} \text{ min}^{-1}$  and  $4.93 \cdot 10^{-4} \text{ min}^{-1}$ , respectively.  
373 It is generally expected that 1D nanostructures could improve the photocatalytic performance  
374 by providing enhanced charge carrier properties and therefore reduced charge  
375 recombination.<sup>75</sup> However, in some cases it was revealed that other factors such as the  
376 oxidation state of the WO<sub>3</sub> could significantly reduce the photo-bleaching performance  
377 despite the 1D morphology.<sup>31</sup> Our results confirmed that there was no such inhibiting factor  
378 therefore the nanowire morphology provided an enhanced efficiency over the nanoparticle  
379 morphology in the photocatalytic test.

380 Additionally, the photo-efficiency of the h-WO<sub>3</sub> NWs was comparable to that of the m-WO<sub>3</sub>  
381 NPs showing similar rate constant values of  $1.72 \cdot 10^{-3} \text{ min}^{-1}$  and  $1.79 \cdot 10^{-3} \text{ min}^{-1}$ , respectively.  
382 The monoclinic phase WO<sub>3</sub> was reported to exhibit higher photo-efficiency relative to  
383 hexagonal WO<sub>3</sub> due to the more oxidized composition<sup>42</sup>, which was confirmed by our results  
384 when h-WO<sub>3</sub> and m-WO<sub>3</sub> NPs with similar morphologies were compared. Clearly, beside the  
385 prominent effect of the crystal phase, the morphology could play an important role in the  
386 determination of the photo-efficiency. The highest photo-degradation was presented by the h-  
387 WO<sub>3</sub> NW/TiO<sub>2</sub> nanocomposite. It decomposed 56 % of the original dye concentration by the  
388 end of the 4-hour reaction, which represents a higher than four times improvement relative to  
389 the h-WO<sub>3</sub> NPs and almost two times better performance relative to the h-WO<sub>3</sub> NWs.  
390 Therefore, the highest rate constant of  $4.22 \cdot 10^{-3} \text{ min}^{-1}$  was calculated for the h-WO<sub>3</sub> NW/TiO<sub>2</sub>  
391 nanocomposite. The enhanced photoactivity can be attributed to the better light utilization  
392 due to absorption in the complete UV-Vis spectrum, and reduced recombination of the photo-  
393 generated charges through effective charge separation between h-WO<sub>3</sub> and TiO<sub>2</sub>. In the  
394 literature it was earlier reported that m-WO<sub>3</sub>-TiO<sub>2</sub> nanocomposite prepared by depositing  
395 TiO<sub>2</sub> onto nanofibers of m-WO<sub>3</sub> by ALD showed improved activities relative to bare WO<sub>3</sub>  
396 and TiO<sub>2</sub>.<sup>45</sup> However, successful ALD reaction onto h-WO<sub>3</sub> NWs to prepare h-WO<sub>3</sub>  
397 NW/TiO<sub>2</sub> nanocomposite has not yet been presented to the best of our knowledge. The  
398 advantage of coupling WO<sub>3</sub> with TiO<sub>2</sub> in various crystal phases and morphologies was shown  
399 to have a great potential in improving photocatalytic performances.<sup>35, 76, 77</sup> This was not  
400 straightforward, since previously it was observed that in the case of blue h-WO<sub>3</sub> samples with  
401 partially reduced W atoms the photocatalytic activity was significantly lower, even compared  
402 to yellow h-WO<sub>3</sub> NPs.<sup>42</sup> The reason could be that although the blue h-WO<sub>3</sub> had absorption in

403 the complete UV-Vis spectrum, this was overcome by that the partially reduced W atoms  
404 served as recombination centers for photo-generated electrons and holes.  
405 Nevertheless, in the case of the h-WO<sub>3</sub>/TiO<sub>2</sub> NW sample, the addition of TiO<sub>2</sub> strongly  
406 influenced the photocatalytic activity, and resulted in a more effective photocatalyst  
407 compared to pure h-WO<sub>3</sub> or m-WO<sub>3</sub>. It clearly shows the efficiency of ALD to reprogramme  
408 the surface properties of nanostructures by depositing nanolayers or nanoparticles on them,  
409 and thus to prepare photocatalysts with superior properties.

410

411

412 *Mechanism of photocatalytic activities.* It was revealed that m-WO<sub>3</sub> nanostructures typically  
413 overperform h-WO<sub>3</sub> nanostructures.<sup>42</sup> It is believed that structural differences play a key role  
414 in that. Photoluminescence studies (PL) confirmed that although h-WO<sub>3</sub> and m-WO<sub>3</sub> has  
415 similar emission pattern, h-WO<sub>3</sub> typically shows lower intensities in the luminescence  
416 spectrum.<sup>42</sup> This was previously attributed to the partially reduced state of h-WO<sub>3</sub> compared  
417 to m-WO<sub>3</sub> which arose from the presence of stabilizing cations in its hexagonal crystal  
418 structure. Between the reduced W atoms polaron transition could take place induced by the  
419 absorbed light.<sup>78</sup> Due to this, fewer light portion can actually play role in the excitation of  
420 electrons from the valence band to the conduction band of the h-WO<sub>3</sub> which explains the  
421 somewhat limited photocatalytic activities of h-WO<sub>3</sub> relative to m-WO<sub>3</sub>.

422 One approach to mitigate e<sup>-</sup>-h<sup>+</sup> pair recombination in single nanostructures is to form  
423 heterojunctions. In the event of beneficially aligned energy levels, the photo-generated  
424 charges can accumulate on different semiconductors which was found to produce longer-  
425 lived charges.<sup>26</sup> For a WO<sub>3</sub>/TiO<sub>2</sub> system the electrons would favor to accumulate on the  
426 conduction band of WO<sub>3</sub> whereas holes would be preferably injected from the valence band  
427 of WO<sub>3</sub> to the valence band of TiO<sub>2</sub>. This way the separation of the photo-generated charges  
428 can take place which supports photocatalytic surface reaction to take place. PL studies were  
429 also applied earlier to confirm the effective charge-separation in WO<sub>3</sub>-TiO<sub>2</sub> systems.<sup>67</sup> It was  
430 found that the emission intensities for the nanocomposite versus eg. TiO<sub>2</sub> was much lowered  
431 which was explained by the improved charge separation in the nanocomposite material.

432

## 433 **Conclusions**

434

435 In this paper h-WO<sub>3</sub> has been prepared by controlled annealing of (NH<sub>4</sub>)<sub>x</sub>WO<sub>3</sub> and by  
436 microwave hydrothermal synthesis to produce nanoparticles and nanowires, respectively. The

437 two distinct morphologies were tested in photocatalytic application against m-WO<sub>3</sub>  
438 nanoparticles prepared also from (NH<sub>4</sub>)<sub>x</sub>WO<sub>3</sub>. The h-WO<sub>3</sub> and m-WO<sub>3</sub> NPs were pure and  
439 consisted of 50-70 nm and 70-90 nm particles, respectively. The h-WO<sub>3</sub> NWs were single  
440 crystalline, 5-10 nm thick and several micrometer long. It was found that the h-WO<sub>3</sub> NWs  
441 had double as high photocatalytic activity compared to h-WO<sub>3</sub> NPs, and their performance  
442 was similar to m-WO<sub>3</sub> NPs.

443 The h-WO<sub>3</sub> nanowires were then used as substrates for TiO<sub>2</sub> deposition by atomic layer  
444 deposition to study the nucleation characteristics of TiO<sub>2</sub> on hexagonal phase WO<sub>3</sub> for the  
445 first time. It was shown that the nucleation on the surface of h-WO<sub>3</sub> was substantially  
446 different from that of the m-WO<sub>3</sub>. When TiO<sub>2</sub> was deposited by ALD onto h-WO<sub>3</sub> NWs, it  
447 did not form a continuous layer as on the surface of m-WO<sub>3</sub>, but rather 5-10 nm particles.  
448 The unique nucleation pattern was understood by the lower surface OH density of h-WO<sub>3</sub>  
449 compared to m-WO<sub>3</sub> which did not serve dense enough nucleation sites for the ALD  
450 reactions to occur in a continuous manner. It was also presented that in contrast to yellow h-  
451 WO<sub>3</sub> NWs, the h-WO<sub>3</sub>/TiO<sub>2</sub> NW turned to blue, due to the appearance of partially reduced W  
452 atoms. Our study is the first investigation of ALD nucleation on various WO<sub>3</sub> polymorphs  
453 and also the first example that different crystalline modifications of the same oxide material  
454 have so diverse effect on ALD growth.

455 When TiO<sub>2</sub> was grown on h-WO<sub>3</sub> NWs, it significantly increased the photocatalytic  
456 degradation rate, and resulted in a 65 % increase in photocatalytic performance. Our results  
457 show that ALD is an outstanding tool to prepare composite photocatalysts.

458

#### 459 **Acknowledgements**

460

461 D. Nagy acknowledges the Principal Career Development Scholarship awarded by the  
462 University of Edinburgh. I. M. Szilágyi acknowledges a János Bolyai Research Fellowship of  
463 the Hungarian Academy of Sciences and an OTKA-PD-109129 grant. Z. Baji, A.L. Tóth are  
464 acknowledged for contributing to the ALD depositions, ellipsometry and SEM-EDX  
465 measurements (Hungarian Academy of Sciences, Centre for Energy Research, Institute of  
466 Technical Physics and Materials Science, Budapest, Hungary).

#### 467 **References**

468

469 1. H. Zhu and T. Lian, *Energy & Environmental Science*, 2012, **5**, 9406-9418.

- 470 2. R. Das, S. B. Abd Hamid, M. E. Ali, A. F. Ismail, M. S. M. Annuar and S.  
471 Ramakrishna, *Desalination*, 2014, **354**, 160-179.
- 472 3. H. Tong, S. X. Ouyang, Y. P. Bi, N. Umezawa, M. Oshikiri and J. H. Ye, *Adv. Mater.*,  
473 2012, **24**, 229-251.
- 474 4. J. Byrne, P. Dunlop, J. Hamilton, P. Fernández-Ibáñez, I. Polo-López, P. Sharma and  
475 A. Vennard, *Molecules*, 2015, **20**, 5574.
- 476 5. N. Zhou, V. Lopez-Puente, Q. Wang, L. Polavarapu, I. Pastoriza-Santos and Q.-H.  
477 Xu, *RSC Adv.*, 2015, **5**, 29076-29097.
- 478 6. W. Wu, J. Changzhong and V. A. L. Roy, *Nanoscale*, 2015, **7**, 38-58.
- 479 7. W. Zhong, D. Li, S. Jin, W. Wang and X. Yang, *Appl. Surf. Sci.*, 2015, **356**, 1341-  
480 1348.
- 481 8. S. Yurdakal, V. Loddo, V. Augugliaro, H. Berber, G. Palmisano and L. Palmisano,  
482 *Catal. Today*, 2007, **129**, 9-15.
- 483 9. S. Malato, P. Fernández-Ibáñez, M. I. Maldonado, J. Blanco and W. Gernjak, *Catal.*  
484 *Today*, 2009, **147**, 1-59.
- 485 10. X. B. Chen, L. Liu, P. Y. Yu and S. S. Mao, *Science*, 2011, **331**, 746-750.
- 486 11. G. Halasi, I. Ugrai and F. Solymosi, *J. Catal.*, 2011, **281**, 309-317.
- 487 12. M. Gratzel, *Nature*, 2001, **414**, 338-344.
- 488 13. Q. Gu, J. L. Long, Y. G. Zhou, R. S. Yuan, H. X. Lin and X. X. Wang, *J. Catal.*,  
489 2012, **289**, 88-99.
- 490 14. A. Fujishima, X. T. Zhang and D. A. Tryk, *Surf. Sci. Rep.*, 2008, **63**, 515-582.
- 491 15. O. Czakkel, E. Geissler, M. Szilágyi Imre and K. László, *Journal*, 2013, **1**, 23.
- 492 16. S. Banerjee, D. D. Dionysiou and S. C. Pillai, *Applied Catalysis B: Environmental*,  
493 2015, **176-177**, 396-428.
- 494 17. Y. Zhang, Z. Jiang, J. Huang, L. Y. Lim, W. Li, J. Deng, D. Gong, Y. Tang, Y. Lai  
495 and Z. Chen, *RSC Adv.*, 2015, **5**, 79479-79510.
- 496 18. K. Teramura, T. Tanaka, M. Kani, T. Hosokawa and T. Funabiki, *J Mol Catal a-*  
497 *Chem*, 2004, **208**, 299-305.
- 498 19. T. Arai, M. Yanagida, Y. Konishi, Y. Iwasaki, H. Sugihara and K. Sayama, *Catal.*  
499 *Commun.*, 2008, **9**, 1254-1258.
- 500 20. Z.-G. Zhao and M. Miyauchi, *Angew. Chem. Int. Ed.*, 2008, **47**, 7051-7055.
- 501 21. D. S. Bohle and C. J. Spina, *J. Am. Chem. Soc.*, 2009, **131**, 4397-4404.
- 502 22. K. Tang, J. Zhang, W. Yan, Z. Li, Y. Wang, W. Yang, Z. Xie, T. Sun and H. Fuchs, *J.*  
503 *Am. Chem. Soc.*, 2008, **130**, 2676-2680.
- 504 23. G. Panthi, M. Park, H.-Y. Kim, S.-Y. Lee and S.-J. Park, *Journal of Industrial and*  
505 *Engineering Chemistry*, 2015, **21**, 26-35.
- 506 24. W. W. Zhong, Y. F. Lou, S. F. Jin, W. J. Wang and L. W. Guo, *Sci Rep*, 2016, **6**.
- 507 25. Z.-F. Huang, J. Song, L. Pan, X. Zhang, L. Wang and J.-J. Zou, *Adv. Mater.*, 2015,  
508 **27**, 5309-5327.
- 509 26. Y. J. Wang, Q. S. Wang, X. Y. Zhan, F. M. Wang, M. Safdar and J. He, *Nanoscale*,  
510 2013, **5**, 8326-8339.
- 511 27. R. Bogue, *Sensor Rev*, 2014, **34**, 1-8.
- 512 28. D. L. Liao, C. A. Badour and B. Q. Liao, *Journal of Photochemistry and*  
513 *Photobiology A: Chemistry*, 2008, **194**, 11-19.
- 514 29. H. Y. Wang, Y. Yang, X. Li, L. J. Li and C. Wang, *Chin. Chem. Lett.*, 2010, **21**,  
515 1119-1123.
- 516 30. M. Reza Gholipour, C.-T. Dinh, F. Beland and T.-O. Do, *Nanoscale*, 2015, **7**, 8187-  
517 8208.
- 518 31. D. Nagy, D. Nagy, I. M. Szilágyi and X. Fan, *RSC Adv.*, 2016, **6**, 33743-33754.
- 519 32. F. Amano, E. Ishinaga and A. Yamakata, *J. Phys. Chem. C*, 2013, **117**, 22584-22590.

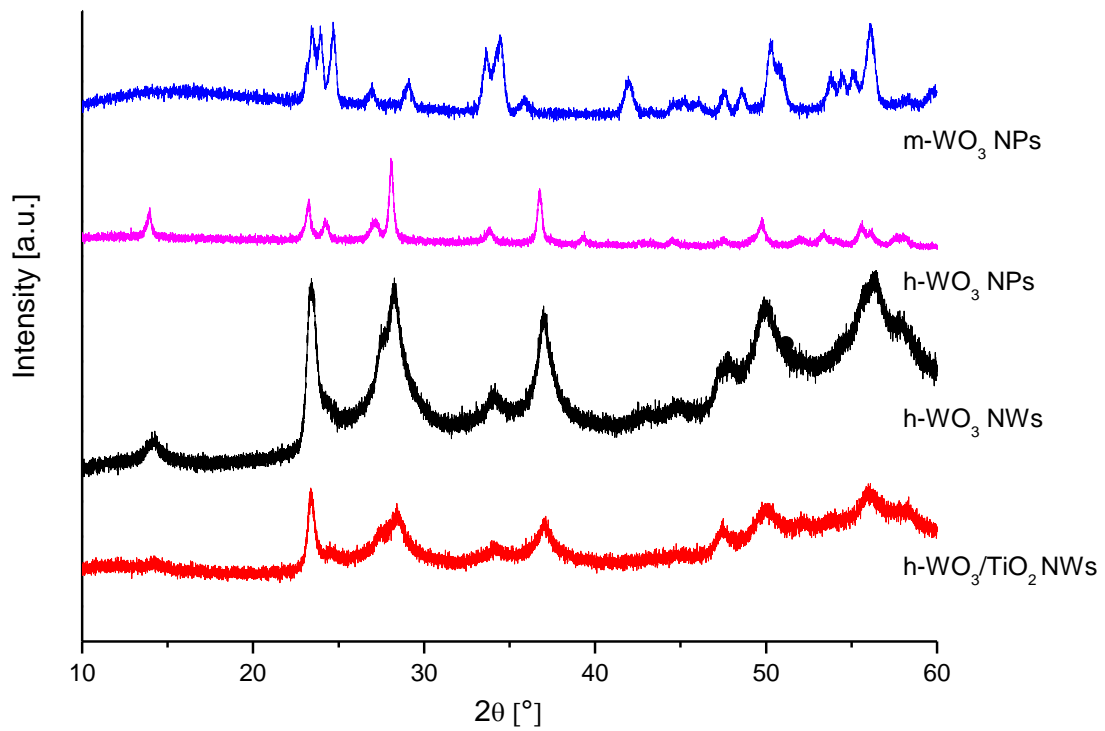


- 520 33. Y. Xia, P. Yang, Y. Sun, Y. Wu, B. Mayers, B. Gates, Y. Yin, F. Kim and H. Yan,  
521 *Adv. Mater.*, 2003, **15**, 353-389.
- 522 34. F. B. Firkala Tamás, Drotár Eszter, Tompos András, Tóth Attila, Varga Josepovits  
523 Katalin, László Krisztina, Leskela Markku, Szilágyi Imre Miklós, *Catal. Lett.*, 2013.
- 524 35. F. Wang, X. Chen, X. Hu, K. S. Wong and J. C. Yu, *Sep. Purif. Technol.*, 2012, **91**,  
525 67-72.
- 526 36. Z. D.-F. MENG Shu-Qian, ZHU Xiao-Fei, YANG Guo-Cheng, LI Zhao-Hui, *Journal*  
527 *of Inorganic Materials*, 2014, **29**, 605-613.
- 528 37. B. Lu, X. Li, T. Wang, E. Xie and Z. Xu, *Journal of Materials Chemistry A*, 2013, **1**,  
529 3900-3906.
- 530 38. L. T. M. P. Guo, C. H. Wang, *Advanced Materials Research*, 2013, **850-851**, 78-81.
- 531 39. E. Kamali Heidari, E. Marzbanrad, C. Zamani and B. Raissi, *Nanoscale Res. Lett.*,  
532 2010, **5**, 370-373.
- 533 40. H. Long, W. Zeng and H. Zhang, *J Mater Sci: Mater Electron*, 2015, **26**, 4698-4707.
- 534 41. I. M. Szilágyi, E. Santala, M. Heikkilä, M. Kemell, T. Nikitin, L. Khriachtchev, M.  
535 Räsänen, M. Ritala and M. Leskelä, *J. Therm. Anal. Calorim.*, 2011, **105**, 73-81.
- 536 42. I. M. Szilágyi, B. Fórizs, O. Rosseler, Á. Szegedi, P. Németh, P. Király, G. Tárkányi,  
537 B. Vajna, K. Varga-Josepovits, K. László, A. L. Tóth, P. Baranyai and M. Leskelä, *J.*  
538 *Catal.*, 2012, **294**, 119-127.
- 539 43. I. M. Szilágyi, J. Madarász, G. Pokol, P. Király, G. Tárkányi, S. Saukko, J. Mizsei, A.  
540 L. Tóth, A. Szabó and K. Varga-Josepovits, *Chem. Mater.*, 2008, **20**, 4116-4125.
- 541 44. A. Phuruangrat, D. J. Ham, S. J. Hong, S. Thongtem and J. S. Lee, *J. Mater. Chem.*,  
542 2010, **20**, 1683-1690.
- 543 45. S. E. Szilágyi I. M., Heikkilä M., Pore V., Kemell M., Nikitin T., Teucher G., Firkala  
544 T., Khriachtchev L., Räsänen M., Ritala M., Leskelä M., *Chem. Vap. Deposition*,  
545 2013, DOI: 10.1002/cvde.201207037.
- 546 46. V. Miikkulainen, M. Leskela, M. Ritala and R. L. Puurunen, *J. Appl. Phys.*, 2013,  
547 **113**.
- 548 47. M. N. Liu, X. L. Li, S. K. Karuturi, A. I. Y. Tok and H. J. Fan, *Nanoscale*, 2012, **4**,  
549 1522-1528.
- 550 48. I. M. Szilágyi and D. Nagy, *Journal of Physics: Conference Series*, 2014, **559**,  
551 012010.
- 552 49. H. Kim, H. B. R. Lee and W. J. Maeng, *Thin Solid Films*, 2009, **517**, 2563-2580.
- 553 50. I. M. Szilágyi, G. Teucher, E. Härkönen, E. Färm, T. Hatanpää, T. Nikiti, L.  
554 Khriachtchev, M. Räsänen, M. Ritala and M. Leskelä, *Nanotechnology*, 2013, **24**,  
555 245701.
- 556 51. M. Knez, K. Nielsch and L. Niinistö, *Adv. Mater.*, 2007, **19**, 3425-3438.
- 557 52. S. Boyadjiev, V. Georgieva, L. Vergov, B. Zs, F. Gáber and I. M. Szilágyi, *Journal of*  
558 *Physics: Conference Series*, 2014, **559**, 012013.
- 559 53. I. M. Szilágyi, J. Pfeifer, C. Balázs, A. L. Tóth, K. Varga-Josepovits, J. Madarász and  
560 G. Pokol, *J. Therm. Anal. Calorim.*, 2008, **94**, 499-505.
- 561 54. I. M. Szilágyi, S. Saukko, J. Mizsei, A. L. Tóth, J. Madarász and G. Pokol, *Solid State*  
562 *Sciences*, 2010, **12**, 1857-1860.
- 563 55. V. B. Patil, P. V. Adhyapak, S. S. Suryavanshi and I. S. Mulla, *J. Alloys Compd.*,  
564 2014, **590**, 283-288.
- 565 56. T. Peng, D. Ke, J. Xiao, L. Wang, J. Hu and L. Zan, *J. Solid State Chem.*, 2012, **194**,  
566 250-256.
- 567 57. J. Yu, L. Qi, B. Cheng and X. Zhao, *J. Hazard. Mater.*, 2008, **160**, 621-628.
- 568 58. D. Hunyadi, A. Vieira Machado Ramos and I. M. Szilágyi, *J. Therm. Anal. Calorim.*,  
569 2015, **120**, 209-215.

- 570 59. D. Hunyadi, I. Sajó and I. M. Szilágyi, *J. Therm. Anal. Calorim.*, 2014, **116**, 329-337.  
571 60. A. Sonia, Y. Djaoued, B. Subramanian, R. Jacques, M. Eric, B. Ralf and B. Achour,  
572 *Mater. Chem. Phys.*, 2012, **136**, 80-89.  
573 61. S. S. I. M. Szilágyi, J. Mizsei, P. Király, G. Tárkányi, A. Tóth, A. Szabó, K. Varga-  
574 Josepovits, J. Madarász, G. Pokol, *Mater. Sci. Forum*, 2008, **589**, 161-165.  
575 62. I. M. Szilágyi, L. Wang, P.-I. Gouma, C. Balázsi, J. Madarász and G. Pokol, *Mater.*  
576 *Res. Bull.*, 2009, **44**, 505-508.  
577 63. C. Santato, M. Odziemkowski, M. Ulmann and J. Augustynski, *J. Am. Chem. Soc.*,  
578 2001, **123**, 10639-10649.  
579 64. A. Rey, P. García-Muñoz, M. D. Hernández-Alonso, E. Mena, S. García-Rodríguez  
580 and F. J. Beltrán, *Applied Catalysis B: Environmental*, 2014, **154-155**, 274-284.  
581 65. I. M. Szilágyi, I. Sajó, P. Király, G. Tárkányi, A. Tóth, A. Szabó, K. Varga-  
582 Josepovits, J. Madarász and G. Pokol, *J. Therm. Anal. Calorim.*, 2009, **98**, 707-716.  
583 66. J. Zhang, W. Zhang, Z. Yang, Z. Yu, X. Zhang, T. C. Chang and A. Javey, *Sens.*  
584 *Actuators, B*, 2014, **202**, 708-713.  
585 67. H. Shen, I.-R. Je, C.-S. Yuan and C.-H. Hung, *Applied Catalysis B: Environmental*,  
586 2016, **195**, 90-103.  
587 68. N. Dávidné, F. Tamás, F. Xianfeng and S. Imre Miklós, *European Chemical Bulletin*,  
588 2016, **5**, 40-42.  
589 69. C. Y. Y. Cheol Seong Hwang, *Atomic Layer Deposition for Semiconductors*, Springer  
590 New York Heidelberg Dordrecht London, 2014.  
591 70. N. Pinna and M. Knez, *Atomic Layer Deposition of Nanostructured Materials* Wiley-  
592 VCH Verlag & Co. KGaA, Weinheim, Germany, 2011.  
593 71. M. Ritala and M. Leskelä, in *Handbook of Thin Films*, ed. H. S. Nalwa, Academic  
594 Press, Burlington, 2002, DOI: <http://dx.doi.org/10.1016/B978-012512908-4/50005-9>,  
595 pp. 103-159.  
596 72. S. Adhikari and D. Sarkar, *RSC Adv.*, 2014, **4**, 20145-20153.  
597 73. J. Su, X. Feng, J. D. Sloppy, L. Guo and C. A. Grimes, *Nano Lett.*, 2010, **11**, 203-208.  
598 74. G. Liu, L.-C. Yin, J. Wang, P. Niu, C. Zhen, Y. Xie and H.-M. Cheng, *Energy &*  
599 *Environmental Science*, 2012, **5**, 9603-9610.  
600 75. H. Dong, Z. Wu, F. Lu, Y. Gao, A. El-Shafei, B. Jiao, S. Ning and X. Hou, *Nano*  
601 *Energy*, 2014, **10**, 181-191.  
602 76. J. K. Yang, X. T. Zhang, H. Liu, C. H. Wang, S. P. Liu, P. P. Sun, L. L. Wang and Y.  
603 C. Liu, *Catal. Today*, 2013, **201**, 195-202.  
604 77. L. Yang, Z. Si, D. Weng and Y. Yao, *Appl. Surf. Sci.*, 2014, **313**, 470-478.  
605 78. S. H. Lee, H. M. Cheong, C. E. Tracy, A. Mascarenhas, D. K. Benson and S. K. Deb,  
606 *Electrochim. Acta*, 1999, **44**, 3111-3115.

607

608

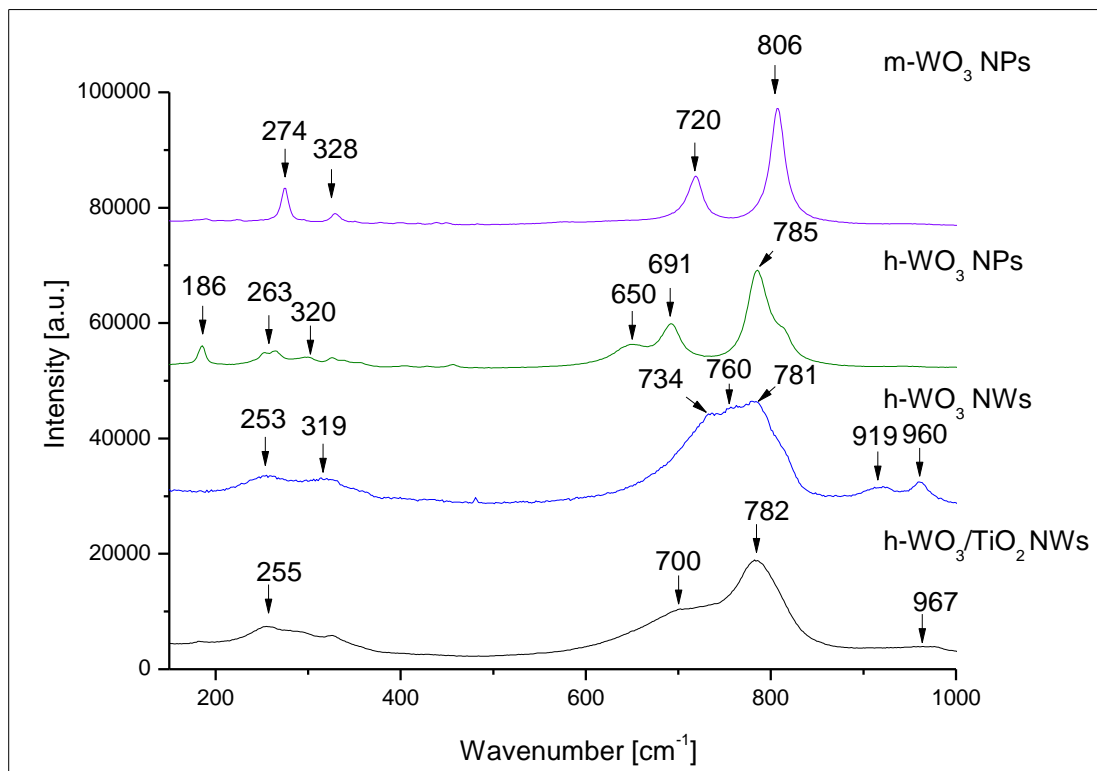


609

610 Figure 1. Powder diffraction pattern of the m-WO<sub>3</sub> NPs, h-WO<sub>3</sub> NPs, m-WO<sub>3</sub> NWs, and h-  
 611 WO<sub>3</sub>/TiO<sub>2</sub> NWs samples

612

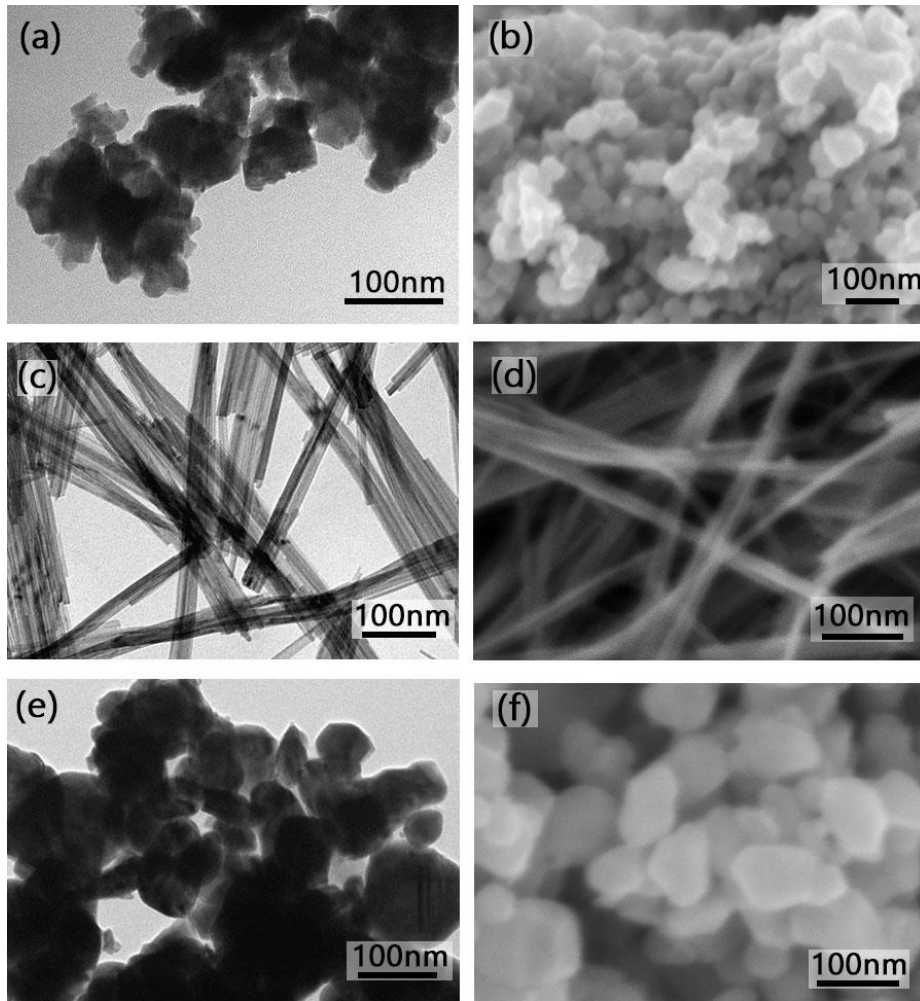
613



614

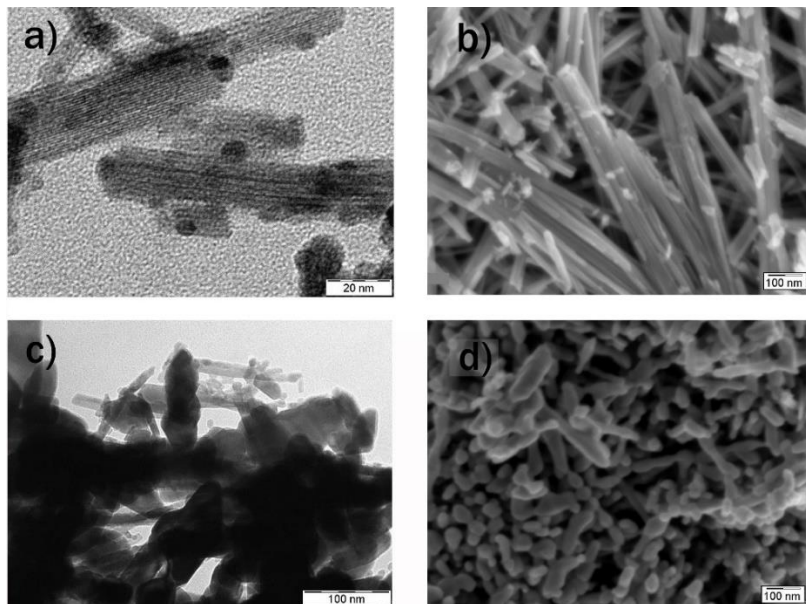
615  
616

Figure 2. Raman spectra of the m-WO<sub>3</sub> NPs, h-WO<sub>3</sub> NPs, m-WO<sub>3</sub> NWs, and h-WO<sub>3</sub>/TiO<sub>2</sub> NWs samples



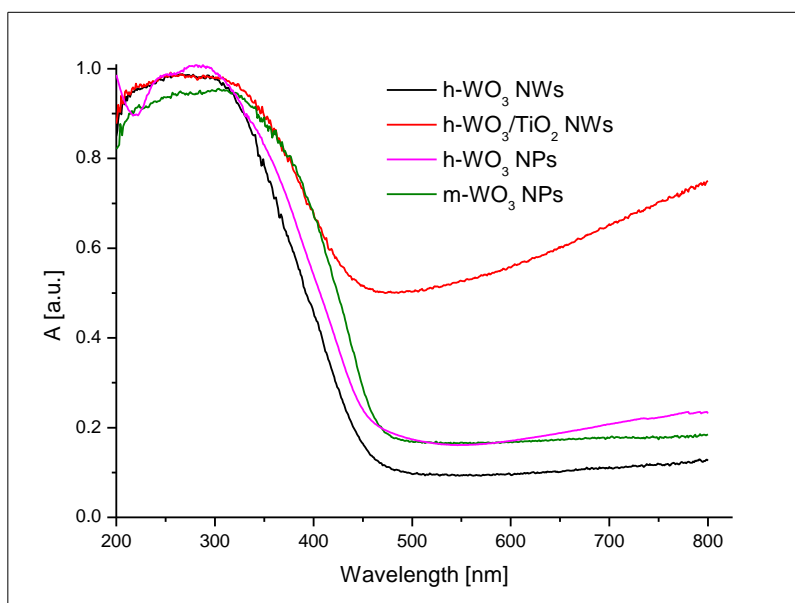
617  
618  
619

Figure 3 TEM and SEM images, respectively, of the prepared samples (a, b) h-WO<sub>3</sub> NPs, (c, d) h-WO<sub>3</sub> NWs, (e, f) m-WO<sub>3</sub> NPs



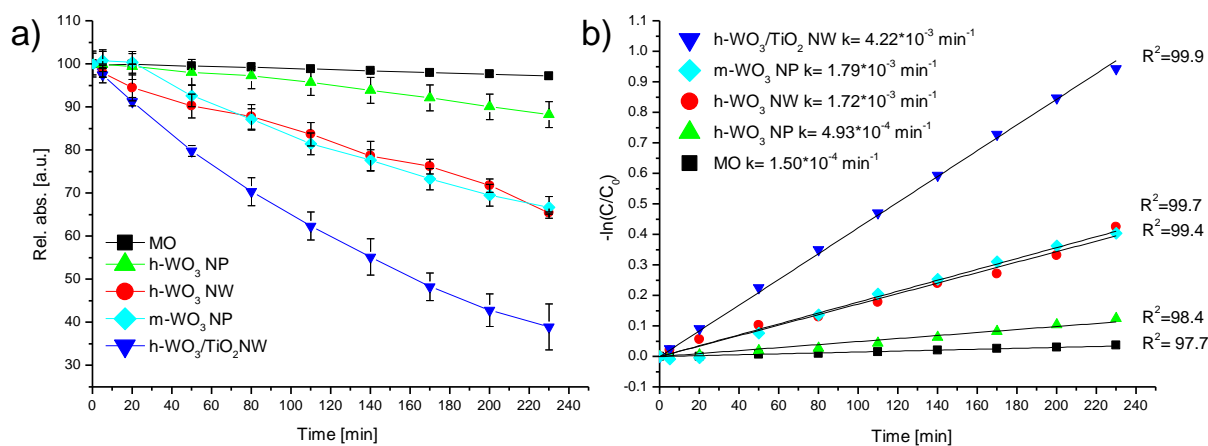
620

621 Figure 4. TEM and SEM images of the (a-b) h-WO<sub>3</sub>/TiO<sub>2</sub> NWs catalyst, (c-d) m-WO<sub>3</sub>/TiO<sub>2</sub>  
 622 samples obtained by annealing h-WO<sub>3</sub>/TiO<sub>2</sub> NWs  
 623



624  
 625 Figure 5. UV-Vis diffuse reflectance spectra of h-WO<sub>3</sub> NWs, h-WO<sub>3</sub> NPs, m-WO<sub>3</sub> NPs and  
 626 h-WO<sub>3</sub>/TiO<sub>2</sub> NWs samples  
 627

628  
 629



630  
 631 Figure 6. a) Photocatalytic degradation curves and b) linearized first rate kinetic curves of the  
 632 m-WO<sub>3</sub> NPs, h-WO<sub>3</sub> NPs, h-WO<sub>3</sub> NWs, and h-WO<sub>3</sub>/TiO<sub>2</sub> NWs samples  
 633